Journal of Magnetism and Magnetic Materials 582 (2023) 170946

Contents lists available at ScienceDirect

Journal of Magnetism and Magnetic Materials

journal homepage: www.elsevier.com/locate/jmmm

Research article

$Co_2Fe(Ti_{0.5}Al_{0.5})$ epitaxial thin films: Structural and magnetic properties of a Heusler alloy with Z-site transition metal substitution

Sujan Budhathoki [a], Anish Rai [a], Ka Ming Law [a], Ridwan Nahar [a], Andrew Stewart [a], Smriti Ranjit [a], Shambhu K.C. [a], Tamara Isaacs-Smith [b], Ilias Bikmukhametov [c], Ryan B. Comes [b], Gregory B. Thompson [d], Patrick R. LeClair [a], Tim Mewes [a], Adam J. Hauser [a,*]

[a] Department of Physics and Astronomy, The University of Alabama, Tuscaloosa, Alabama 35487, USA
[b] Department of Physics, Auburn University, Auburn, Alabama 36849, USA
[c] Alabama Analytical Research Center, The University of Alabama, Tuscaloosa, Alabama 35487, USA
[d] Department of Metallurgical & Materials Engineering, The University of Alabama, Tuscaloosa, Alabama 35487, USA

ARTICLE INFO

Keywords:
Heusler alloys
Spintronics
Ferromagnetic resonance spectroscopy

ABSTRACT

We investigate the structural, static, and dynamic magnetic properties of epitaxial Heusler $Co_2Fe(Ti_{0.5}Al_{0.5})$ (CFTA) alloy thin films with thickness varying from 6 nm to 80 nm grown by sputter beam epitaxy on cubic MgO(001), $MgAl_2O_4(001)$, and hexagonal $Al_2O_3(11\bar{2}0)$ substrates. X-ray diffraction measurements indicate epitaxial growth of CFTA thin films with B2 chemical ordering, with cubic [001] and [220] CFTA axes normal to the cubic and hexagonal substrates, respectively. Microstructure analysis of films grown on MgO substrates reveals a uniformly oriented epitaxial crystal with small variations consistent with strain distortions, providing an explanation for the relatively large X-ray rocking curve values found. Meanwhile, films on $Al_2O_3(11\bar{2}0)$ substrates reveal columnar growth with frequent in-plane grain rotations. A pronounced four-fold magnetocrystalline anisotropy is observed in epitaxial thin films grown on cubic substrates. A pronounced uniaxial anisotropy for films grown on $Al_2O_3(11\bar{2}0)$ substrates is observed. A saturation magnetization of $\sim 5.0\mu_B$/f.u. (where f.u. represents formula unit) is obtained at room temperature, slightly smaller compared to the expected value based on the Slater-Pauling rule. Ferromagnetic resonance spectroscopy finds an effective damping parameter and inhomogeneous linewidth broadening comparable to those found in parent compound Co_2FeAl, which suggests that Ti substitution can be achieved without negatively affecting the magnetic properties of the system.

1. Introduction

Candidate material systems with high spin polarization and low damping parameter are highly sought-after for applications in low power spintronic devices. High spin polarization is a pre-requisite for high tunneling magneto-resistance (TMR) ratios, and a low damping constant implies that a small current density will be required to switch the magnetization [1–3]. These attributes largely dictate the efficiency of spin-transfer torque (STT) [4] and spin-torque oscillators. Half metallic materials with a bandgap at the Fermi level (E_f) for one spin channel are expected to have up to 100% spin-polarized conduction electrons, and are therefore ideal candidates to realize efficient spintronic devices.

Half metallic Heusler compounds are theorized to be promising candidates for spintronic applications based on first principles calculations [5]. The magnetic properties of a given compound can be tuned by elemental choice, which dictates the number of valence electrons and the resultant properties of the system. Heusler alloys have compositions of the form (a) X_2YZ, known as a full Heusler alloy (including the regular Heusler $L2_1$ type structure and the inverse Heusler XA type structure) and (b) XYZ, known as a half Heusler alloy [5,6]. As a rule of thumb, X and Y are transition elements and Y is often a main group element. All the available lattice sites i.e., tetrahedral and octahedral sites in a cubic crystal structure are occupied in the case of a full Heusler alloy, whereas half of the tetrahedral sites remain vacant in the half Heusler alloys. Heusler alloys exhibit a wide range of properties including, but not limited to half metallicity [7], superconductivity [8], and topological properties [9]. With these useful properties, Heusler alloys have unsurprisingly earned significant interest scientifically as well as in device applications.

* Corresponding author.
E-mail address: ahauser@ua.edu (A.J. Hauser).

https://doi.org/10.1016/j.jmmm.2023.170946
Received 26 March 2023; Received in revised form 12 June 2023; Accepted 19 June 2023
Available online 28 June 2023

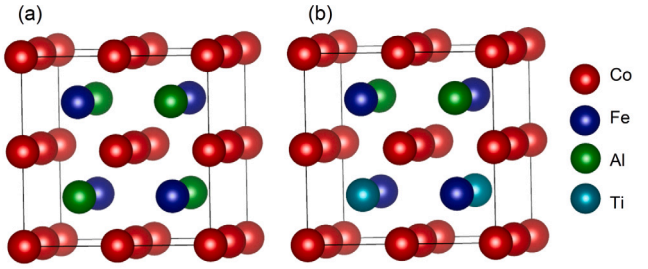

Fig. 1. (a) $L2_1$ structure of Co_2FeAl (b) Possible structure of $Co_2Fe(Ti_{0.5}Al_{0.5})$ formed by substitution of a part of Al atoms by Ti atoms. It should be noted that it is just one of the different possibilities of the resulting substitutional compound.

Co-based Heusler alloys are of particular interest for their high Curie temperature (T_c) exceeding 1000 K [10–15], giant tunneling magnetoresistance (GTMR) effects in magnetic tunnel junctions [16, 17], and low Gilbert damping parameter [18]. However, integration into spintronic devices has been complicated by thermodynamic tendency for chemical disorders that can alter spintronic properties. For instance, the ultralow damping parameter values predicted for ideally ordered Co-based Heusler alloys [19] has not materialized in fabricated samples [20,21], as atomic ordering of even 90% has proven elusive.

Many experimental groups have worked to tune the properties by substitution of either Y-site (by transition element) [22–25] or Z-site (by main group element) [26–28] elements. Experimental work investigating magnetic property modulation via main group element Z-site substitution in Co_2FeAl has been shown to improve spin polarization at room temperature [26–28]. However, the substitution of transition metals into the Z-site, creating electron-like doping, has not been well-studied and the possibility and nature of such substitutions is an open question.

In this letter, we report the structural and magnetic properties resulting from Titanium (Ti) substitution in place of Aluminum (Al) within the Co_2FeAl parent system. Epitaxial thin films of $Co_2Fe(Ti_{0.5}Al_{0.5})$ (hereafter CFTA, structure shown in Fig. 1) thin films were grown on $Al_2O_3(11\bar{2}0)$, MgO(001), and $MgAl_2O_4(001)$ (MAO) substrates via sputter beam epitaxy (SBE) [29–32]. The expected epitaxial orientation of CFTA films on each of the substrates is shown in Fig. 2. We find that titanium can successfully incorporate into the alloy when replacing aluminum, though X-ray diffractometry shows no significant evidence of $L2_1$-type atomic ordering. Despite the nebulous atomic ordering, films still show both (1) a low effective Gilbert damping parameter comparable to the parent compound and (2) a small inhomogeneous linewidth broadening values important to figures of merit for spintronic devices [33]. Films on all three substrates show saturation magnetizations of ~ 5 μ_B/formula unit (f.u.), close to the value expected by the Slater-Pauling rule [13].

2. Sample preparation and experimental methods

A series of CFTA thin films with variable thicknesses (t = 6 nm, 11 nm, 23 nm, 40 nm, 57 nm, and 80 nm) were grown on MgO(001), MAO(001), and $Al_2O_3(11\bar{2}0)$ single-crystal substrates in a 3 mTorr Ar atmosphere by SBE [29–31] in an AJA International, Inc. system with a base pressure 5 × 10^{-9} Torr, and at a substrate temperature of 700 °C. At each thickness, the films were grown simultaneously on all three substrates, and on the same substrate holder. The optimum growth temperature, pressure, and deposition rates were determined by analyzing X-ray diffraction (XRD) film peak intensity, full width at half maximum (FWHM) of rocking curve (RC) measurements about the film peak, and analysis of small-angle X-ray reflectometry (XRR) data. The deposition rate was monitored by a quartz crystal microbalance (QCM) and a growth rate of 1.67 Å/s was used. The sample holder was rotated

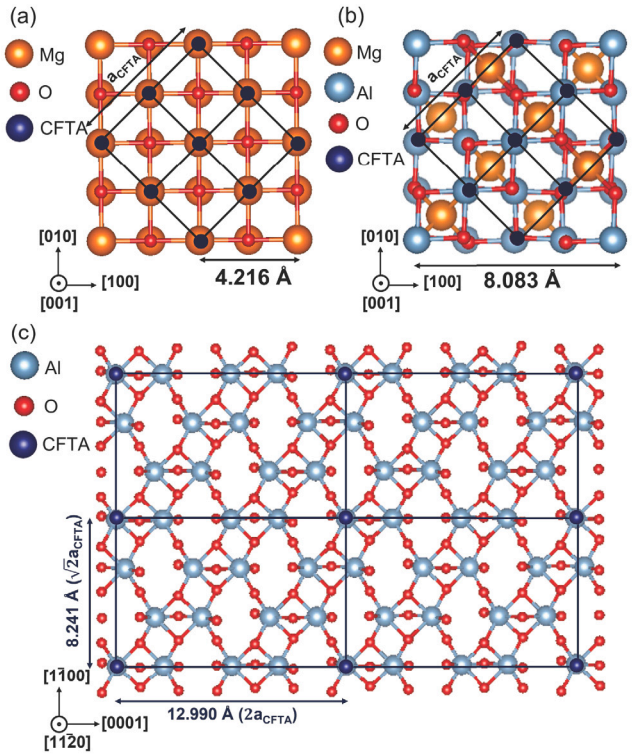

Fig. 2. The expected epitaxial orientation of CFTA thin films on (a) MgO(001) substrate (2 × 2 construction for clarity) i.e., CFTA(001)[011]//MgO(001)[100] and (b) MAO(001) substrate i.e., CFTA(001)[011]//MAO(001)[100] with a 45° rotation on MgO(001) and MAO(001) plane, and (c) $Al_2O_3(11\bar{2}0)$ (a potential epitaxial arrangement of CFTA (110) plane on $(11\bar{2}0)$ plane of Al_2O_3. A 3 × 3 construction of CFTA(110) plane is overlayed on 2 × 2 construction of $(11\bar{2}0)$ plane of Al_2O_3. CFTA atoms are shown only at the unit cell length for visual clarity and the given crystallographic directions correspond to the substrate.

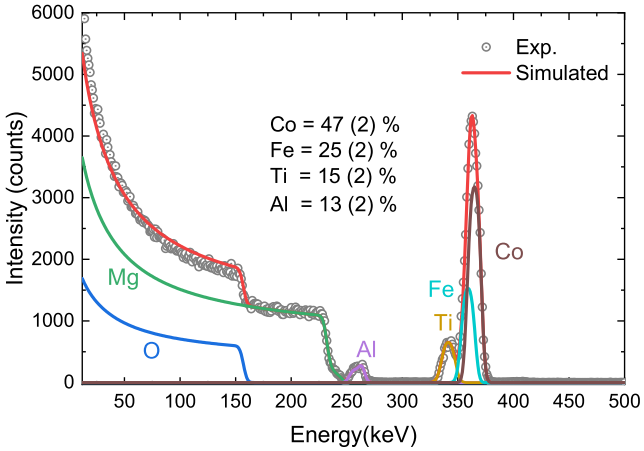

Fig. 3. RBS spectrum of CFTA thin film deposited on MgO(001) substrate showing nearly stoichiometric CFTA films i.e., $Co_{1.88}Fe(Ti_{0.6}Al_{0.52})$ within ±2% accuracy.

at 80 revolutions/minute to ensure homogeneity across the substrate during deposition. Prior to the deposition of the CFTA thin films, the substrates were in-situ annealed at 700 °C for 30 min. Subsequently, CFTA films were deposited at 700 °C and were capped with ~ 3 nm Al layer at 80 °C.

Rutherford backscattering (RBS) was used to confirm the stoichiometry of as-deposited CFTA thin films. The RBS data were collected

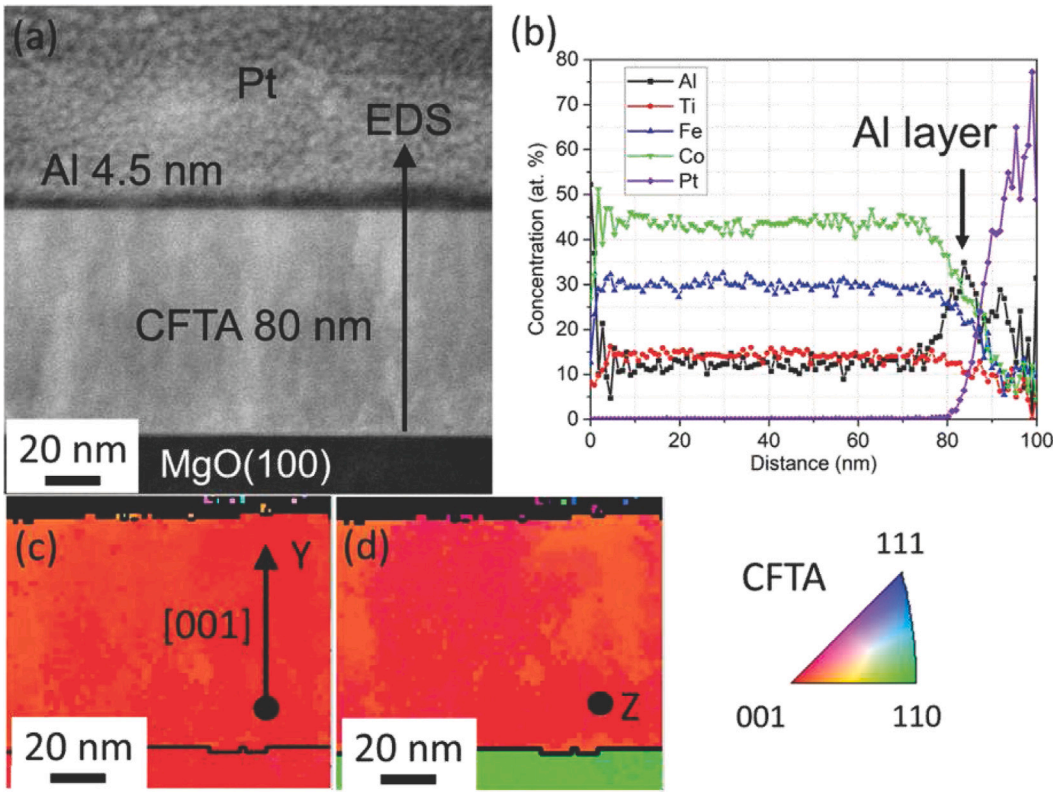

Fig. 4. Cross-section TEM characterization of CFTA thin film grown on MgO(001) substrate: (a) STEM image of the film cross-section; (b) EDS composition profile along the line in (a); (c) Y-orientation (film growth direction) PED map from the same area as (a); (d) Z-orientation (normal to the TEM sample) PED map. The rainbow triangle represents a color key to PED maps.

through Helium ion bombardment using the 6HDS-2 tandem, National Electrostatics Corporation Pelletron at Auburn University, with 2 sources for ions, an alphatross (RF source for production of He^+) and SNICS source (source of negative ions by Cesium sputtering). The microstructure of CFTA films were probed using transmission electron microscopy (TEM). The cross-section TEM samples were characterized in a FEI Tecnai F20 TEM using conventional bright-field (BF) imaging, high-angle annular dark-field imaging (HAADF), precession electron diffraction (PED) and energy dispersive spectroscopy (EDS). Cross-section TEM samples were prepared from 80 nm thick CFTA films deposited on MgO and Al_2O_3 substrates by standard focused ion beam (FIB) lift-out technique [34] using a Tescan Lyra dual FIB – scanning electron microscopy (SEM) unit. PED was used for film orientation mapping and was facilitated by automated NanoMEGAS platform [35]. The PED scans were collected at a step size of 2 nm and a precession angle of 0.375°. PED maps were initially indexed in NanoMEGAS index software using CFTA and Al_2O_3 templates generated by NanoMEGAS diffgen software from .CIF files provided by ICSD database [36].

Then result files were cleaned from potential ambiguities in the NanoMEGAS map viewer software and then exported to TSL OIM v.8 software. Afterward, the grain boundary and grain orientation maps were cleaned using the grain dilation tool with thresholds set to a 5° misorientation angle and 5 nm minimum grain size in a single iteration mode. EDS technique was used to plot compositional profile across the films and was done using EDAX Optima T60 detector in a line scan mode with a step size of 1 nm.

Crystal structure, epitaxial quality, and film thickness were characterized by XRD and XRR using a Philips X-pert X-ray diffractometer using parallel beam optics with a Cu-Kα (λ = 1.5418 Å) radiation source. The static magnetic properties, magnetization at saturation, and hysteresis loops for CFTA thin films at room temperature were investigated using the VSM module in a Quantum Design Physical Property Measurement System (PPMS). Room temperature broadband ferromagnetic resonance (FMR) measurements were carried out using a custom-designed coplanar wave-guide system to probe the dynamic properties of CFTA thin films. In-plane (IP) angular-dependent measurements at a fixed frequency of 20 GHz were carried out as well using FMR spectroscopy, to obtain information about the magnetic anisotropy of the sample. The derivative of a Lorentzian line shape [37] was used to fit the raw FMR spectra to determine the resonance field (H_{res}) and the peak-to-peak linewidth (ΔH_{pp}) as a function of frequency.

3. Results and discussion

3.1. Structural characterization

RBS data (gray open circles) and simulated fits (elemental contributions as labeled solid lines, total sum as red solid line) of CFTA films are shown in Fig. 3 and show that the films are nearly stoichiometric within experimental uncertainty, with slight cobalt deficiency and slight excess of titanium (47(2) at% Co, 25(2) at% Fe, 15(2) at% Ti, and 13(2) at% Al). HAADF TEM analysis (Fig. 4(a)) of our thickest CFTA film deposited on MgO substrate shows the actual thickness of the CFTA layer to be 80 nm.

Fig. 4(b) shows an EDS compositional profile acquired along the line in Fig. 4(a), there it is observed that the composition across the film was uniform and close to the composition reported above, within the uncertainty of the technique. Small deviations in Fe content are attributed to the errors in TEM EDS characterization of Fe, Fig. 4(b). PED orientation maps are represented here in form of "Y" and "Z"

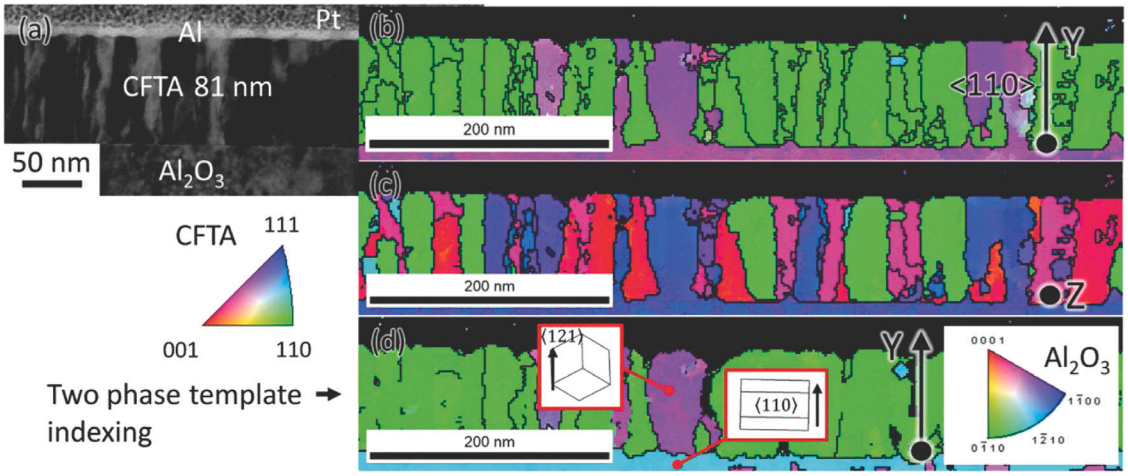

Fig. 5. Cross-section TEM characterization of CFTA thin film grown on Al_2O_3 substrate: (a) BF image of the film cross-section; (b) Y-orientation (growth direction) IPF map from the same area as (a) indexed using only CFTA template; (c) Z-orientation (normal to the TEM sample) IPF map indexed using only CFTA template; (d) Y-orientation (growth direction) IPF map from the same area as (a) indexed using CFTA and Al_2O_3 templates. The rainbow triangles represent color keys to PED maps.

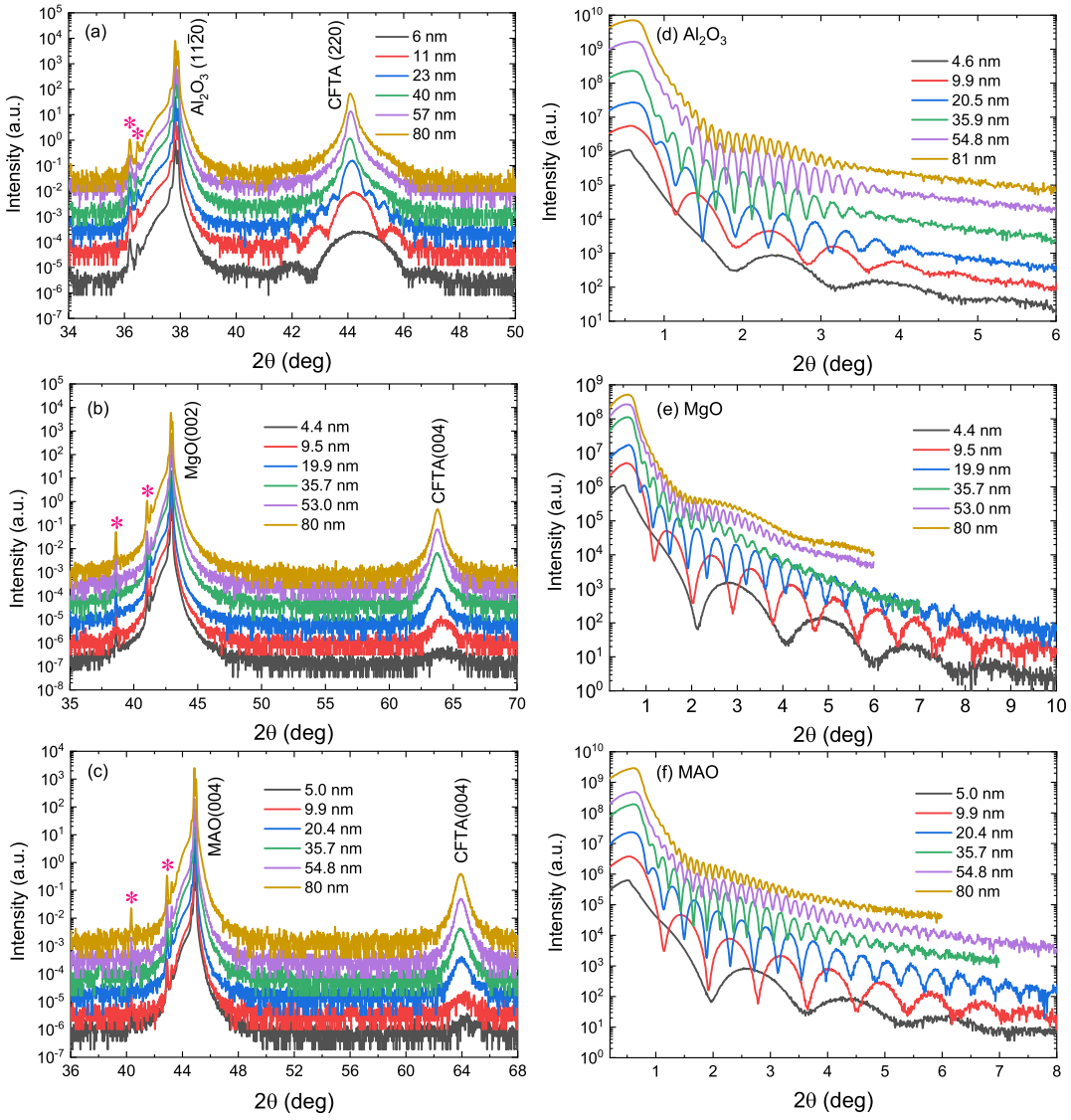

Fig. 6. $2\theta-\omega$ XRD (Cu X-ray source) scans of epitaxial CFTA thin films (vertically offset for clarity) on (a) $Al_2O_3(11\bar{2}0)$ (b) MgO(001), and (c) MAO(001) single crystal substrates. *Asterisks (*) indicate substrate peaks.* $2\theta-\omega$ XRR scans of CFTA films on (d) $Al_2O_3(11\bar{2}0)$ (e) MgO(001) and (f) MAO(001) substrates demonstrate pronounced Kiessig oscillations with actual film thickness shown.

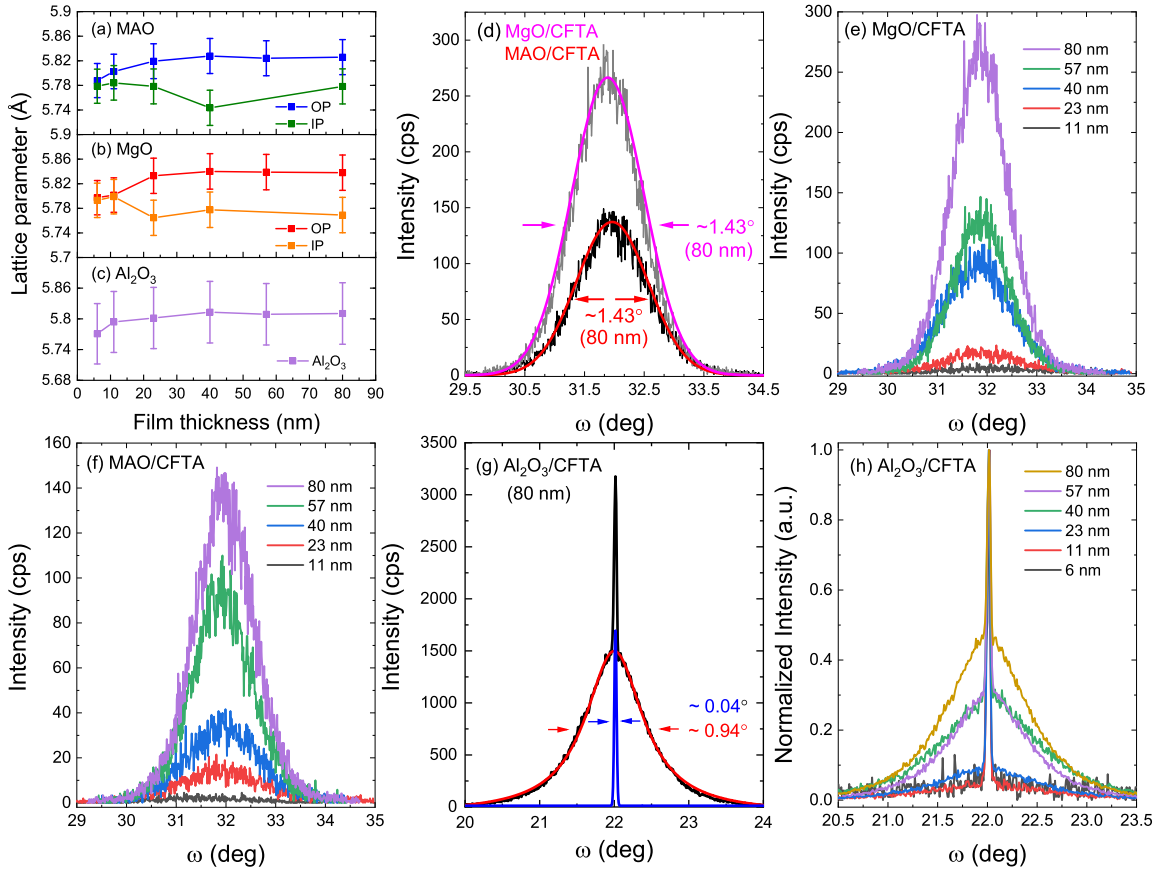

Fig. 7. Variation of out-of-plane (OP) and in-plane (IP) lattice parameters for CFTA thin films with respect to film thickness on (a) MAO, (b) MgO, and (c) Al_2O_3 substrates. The lattice parameters for CFTA thin films on Al_2O_3 substrates are extracted based on the (220) Bragg reflection in the OP direction and shown for comparison. (d) Rocking curve (RC) for (004) Bragg peak of 80 nm thick CFTA film on MgO and MAO substrates. The corresponding fits are shown in magenta (on MgO) and red (on MAO) color with FWHM ~ 1.43°. RCs for (004) Bragg reflections across film thickness for CFTA films grown on (e) MgO and (f) MAO substrates. (g) RC for (220) Bragg peak of 80 nm thick CFTA film on Al_2O_3 substrate showing FWHM for a broad background (FWHM ~ 0.94°) and sharp peak (FWHM ~ 0.04°). (h) Variation of RCs using the normalized intensity showing evolution of peak broadening for (220) Bragg peak across film thickness for CFTA films grown on Al_2O_3 substrate. The broadening almost disappears for thinner films.

inverse pole figure (IPF) maps, where colors represent orientation in a certain point parallel to "Y" or "Z" direction, Fig. 4(c)–(d). The IPF maps in Fig. 4(c)–(d) confirm that CFTA films grown on MgO substrates exhibit the CFTA(001)[011]//MgO(001)[100] epitaxial arrangement shown in Fig. 2(a). The CFTA film grown on MgO substrate was uniform through thickness with orientation deviations not more than 1°, which is the resolution limit for the PED technique.

Fig. 5 represents TEM analysis of CFTA film grown on Al_2O_3 substrate, the thickness of the film was measured to be 81 nm from the BF image shown in Fig. 5(a). Although the films were grown simultaneously, the films grown on MgO and Al_2O_3 show a small but consistent 1 nm thickness difference (shown in Figs. 4(a) and 5(a) respectively), likely due to the error margin of the technique used.

The IPF map shown in Fig. 5(b) shows that the CFTA film on Al_2O_3 substrate has a dominant orientation [110] parallel to the growth direction. However, in contrast to the CFTA film on MgO substrate, the CFTA film on Al_2O_3 substrate contains high-angle grain boundaries, shown in black lines in Fig. 5(b). Additionally, "Z" orientation IPF mapping (Fig. 5(c))) shows significant in-plane grain rotations with at least 4 orientation variants with respect to the substrate (signified by green, red, blue, and magenta colors in the "Z" map). Note that in Figs. 5(b)–(c) the orientations seemingly indicated by colors in the substrate regions should be disregarded, since only the CFTA template was used during indexing to increase indexing quality. The IPF map where both templates (CFTA and Al_2O_3) were used for indexing datasets is shown in Fig. 5(d), here could be noted that a single growth variant is deviated from <110> growth having CFTA (121) plane on $Al_2O_3(11\bar{2}0)$ arrangement.

Fig. 6(a)–(c) show the out-of-plane (OP) X-ray $2\theta-\omega$ XRD diffraction patterns for CFTA thin films, with variable thicknesses (t = 6 nm, 11 nm, 23 nm, 40 nm, 57 nm, and 80 nm), on (a) $Al_2O_3(11\bar{2}0)$, (b) MgO(001), and (c) MAO(001) substrates. Similarly, Fig. 6(d)–(e) show small angle XRR for CFTA thin films grown on Al_2O_3, MgO, and MAO substrates, respectively. From XRR, we observe pronounced Kiessig oscillations, typical to atomically abrupt and smooth air-film and film-substrate interface, due to the thickness of the CFTA film. The presence of pronounced Laue oscillations on thinner films grown on Al_2O_3 substrates as shown in Fig. 6(a) indicate atomically flat and smooth interfaces. In particular, we observe a systematic shift in (220) Bragg peak, Fig. 6(a), towards a higher angle with decrease in thickness from 40 nm indicating a tensile strain in thinner films. We observe a similar feature in (004) Bragg peaks in XRD scans for films grown on MgO, Fig. 6(b) and MAO, Fig. 6(c) substrates.

The variation of OP lattice parameter for CFTA thin films with respect to film thickness is shown in Fig. 7(a), (b), and (c). After a film thickness of 40 nm, CFTA films relax to bulk ~ 5.8 Å evidenced from the observed XRD pattern and plot of extracted lattice parameter against the film thickness in Fig. 7. The observed lattice parameters are larger for films grown on MgO (a_{MgO} = 4.216 Å) compared to MAO (a_{MAO} = 8.083 Å) substrates, consistent with the expected larger

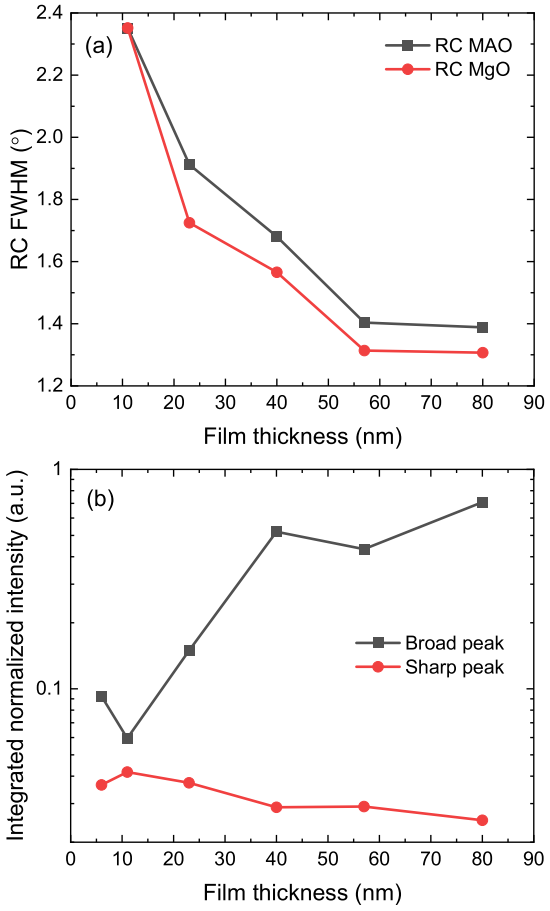

Fig. 8. (a) Evolution of RC FWHM with film thickness for CFTA thin films on MgO(001) and MAO(001) substrates (b) Plot of the integrated normalized intensity (normalized to peak intensity) for broad and sharp peaks in the RC for CFTA (220) Bragg reflection for films grown on Al_2O_3 substrate as a function of film thickness. Each peak/curve is fitted using a Voigt function to estimate the integrated area underneath the curve.

lattice strain from MgO substrates. The error bar for the extracted lattice parameters for CFTA films on Al_2O_3 substrate is higher as the lattice parameters were calculated based on (220) Bragg reflection from the off-axis measurements (explained later in the text). From the XRD results, we observe that the CFTA films have a tetragonal symmetry due to IP epitaxial strain.

The RC scan, the plot of scattered X-ray intensity versus ω, of CFTA Bragg peaks are shown in Fig. 7(d), (e), and (f). The RC dictates the broadening of Bragg peaks due to mosaic spread, misfit dislocations, stress/strain encompassing the dislocations, and a distribution of crystal inter-planar d-spacings [38]. Mosaicity quantifies the distribution of crystallites with different tilt angles with respect to each other. It should be noted that each mosaic counterpart can satisfy Bragg's condition and eventually give rise to the variation of intensity. A sharp RC is indicative of well aligned crystallites, whereas a broad RC indicates crystal imperfections. The RC FWHM of CFTA(004) Bragg peak is estimated to be ~ 1.43° for 80 nm thick films grown on MgO and MAO substrates as shown in Fig. 7(d).

Similarly, the RC for CFTA films grown on Al_2O_3 substrates are shown in Fig. 7(g) and (h). Unlike films grown on MAO and MgO substrates, the RCs for films grown on Al_2O_3 substrates show two distinct peak features - a sharp peak feature is observed to overlay on a broader background. These two shapes i.e the sharp peak and broad background in RC possibly indicate the strained and relaxed portion of the films respectively. The FWHM for the sharp peak is estimated

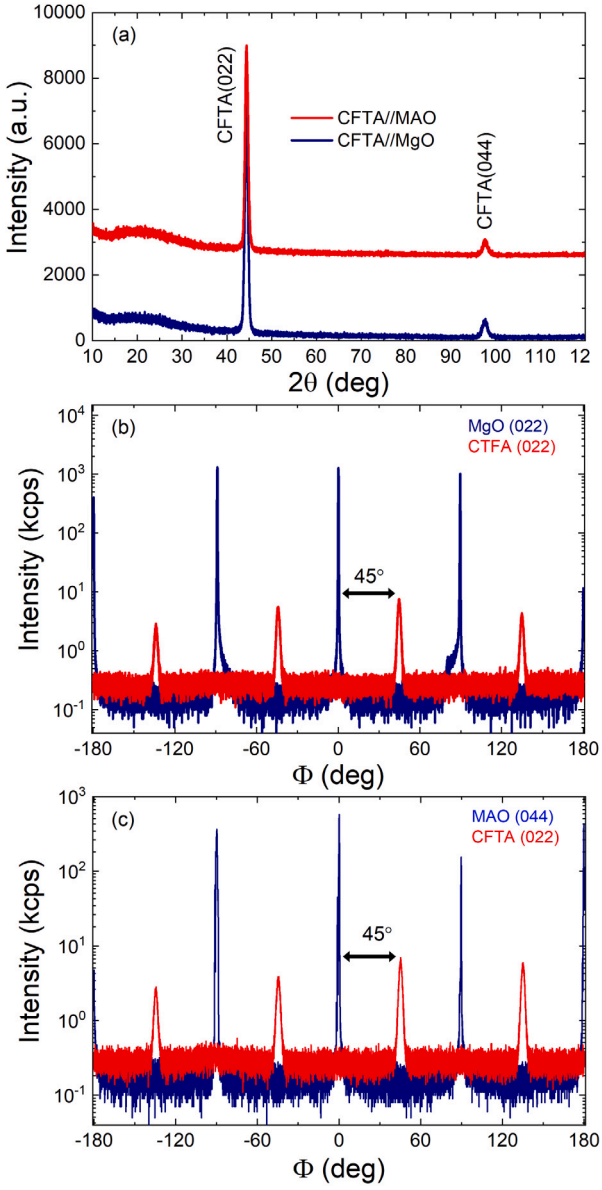

Fig. 9. (a) $2\theta - \omega$ XRD (Cu X-ray source) off-axis scans (vertically offset for clarity) of 23 nm thick CFTA film on MgO (navy) and MAO (red) showing (022) and (044) Bragg reflection to determine in-plane (IP) lattice parameter. ϕ-scan of the CFTA(022) film peak at a tilt angle $\psi = 45°$ with respect to (b) MgO(001) substrate (c) MAO(001) substrate demonstrate the expected epitaxial relationship.

to be ~ 0.04°, whereas ~ 0.94° for broad background for 80 nm thick film grown on Al_2O_3 substrate as shown in Fig. 7(g). The FWHM for the 6 nm thick film is ~ 0.04°. The peak broadening increases with thickness, suggesting that tilted crystallites, misfit dislocations, and strain become a large fraction of the film as one move away from the surface for films grown on Al_2O_3 substrate as shown in Fig. 7(h). However, the RC FWHM for CFTA(004) films grown on MgO(001) and MAO(001) substrate progressively decreases with film thickness as shown in Fig. 8(a) indicating <001> oriented CFTA films with improved uniformity and coordination between crystallites as they grow upward. The evolution of integrated intensity of both the sharp and broad peaks for films grown on Al_2O_3 substrate as a function of film thickness is shown in Fig. 8(b). Both the broad and sharp peaks/features on the RC were fitted using a Voigt function to estimate the area under

each curve. We can see from Fig. 8(b) that the area underneath the broad curve increases with film thickness, whereas the area underneath the sharp peak feature remains relatively constant.

The sharp peak feature in the RC as shown Fig. 7(g) and (h) is indicative of a highly oriented and strained portion of the films also evident from Fig. 8, whereas the broad background is likely due to the misfit dislocations to relieve strain causing diffuse scattering [39,40]. The IP orientation spread as shown in Fig. 5(c) likely also contributes to the observed broadening in the RC. At 6 nm thickness, the contribution from the broad background almost vanishes possibly indicating a fully strained film. Further, we can see from Fig. 7(a), (b), and (c) that the CFTA films relax after 40 nm, which explains the increased share of the broad peaks on RCs as lattice distortion causes strain-relaxation. Unlike films grown on Al_2O_3 substrates, the films grown on MgO and MAO substrates do not exhibit two peak features indicating that the films on MgO and MAO are highly oriented. The pronounced Laue and Kiessig oscillations in XRD and XRR patterns indicate a very smooth interface, and a low RC FWHM indicates highly oriented and uniform films.

For Heusler systems, the non-zero Bragg reflections occur if and only if the Miller indices are either all odd, or all even. Strictly speaking, the introduction of a transition metal to the Z-site, where element choices are typically limited to the p-block, prevents a clean classification of CFTA as a Heusler alloy. However, tests for $L2_1$-type structure are warranted given the novelty of the substitution herein. We do not observe odd Miller indices in our films, including 111 superlattice or 311 diffraction peaks, likely ruling out the possibility of significant $L2_1$-like phase in our films. We observed 400 reflection and 220 principle reflections across all films in MgO and MAO substrates. A 220 principle reflection is seen in films grown on Al_2O_3 substrates evidenced from Fig. 6(a). The presence of even Miller indices hints towards either a B2 or an A2 phase across the films. A B2 phase corresponds to randomness across Y i.e., Fe and Z-sites i.e., Ti and Al in our case. Whereas an A2 phase corresponds to randomness across all the available sites i.e., X, Y, and Z. The structure factor analysis, $F_{hkl} = \sum_n f_n e^{2\pi i(hx_n+ky_n+lz_n)}$, where $n\ \epsilon\ (A, B, C, D)$ for the atomic positions $A = (0,0,0)$, $B = (1/4, 1/4, 1/4)$, $C = (1/2, 1/2, 1/2)$, $D = (3/4, 3/4, 3/4)$ and f_n is the average scattering factor on the n sites [41], suggests a low level of A2 disorder as we observe 200 superlattice peak on films grown on MgO and MAO substrates and hints towards a likelihood of B2 phase of our films. However, it should be noted that an additional local atomic disorder between Co and Fe atoms either by partial occupancy of the Fe sites with Co atoms or site swapping of Co and Fe atoms (which have very similar electronegativity and atomic radii and are typically prone to site-swapping) cannot be ruled out from this analysis.

The IP lattice parameters for films grown on cubic substrates were calculated based on (044) Bragg reflection of CFTA films at a tilt angle $\psi = 45°$ by off-axis XRD measurement as shown in Fig. 9(a) on MgO and MAO substrates respectively. The on-axis ($\psi = 0°$) diffraction measurements gave an OP lattice d-spacing of 1.458 Å ± 0.007 Å (1.455 Å ± 0.007 Å) for (004) Bragg reflection for 23 nm thick films on MgO (MAO) substrates, respectively. The corresponding OP lattice parameter (c) was determined to be 5.834 Å ± 0.028 Å (5.819 Å ± 0.028 Å) for 23 nm thick films on MgO (MAO) substrates. Similarly, the OP lattice parameter for other films were evaluated. At a tilt angle $\psi = 45°$, the OP lattice d-spacing was found to be 2.042 Å ± 0.021 Å (2.039 Å ± 0.021 Å) for (022) Bragg reflection and 1.025 Å ± 0.001 Å (1.025 Å ± 0.001 Å) for (044) Bragg reflection for 23 nm thick films grown on MgO (MAO), respectively. Then, using the (044) Bragg reflection d-spacing for a tetragonal lattice i.e., $\frac{1}{d_{440}^2} = \frac{h^2+k^2}{a^2} + \frac{l^2}{c^2}$ with c being the OP lattice parameter calculated based on (004) Bragg reflection and a being the IP lattice parameter, the IP lattice parameter (a) was determined to be 5.764 Å ± 0.028 Å (5.778 Å ± 0.028 Å) on MgO (MAO) substrates, respectively for 23 nm thick CFTA films. Similarly, the lattice parameters for other films were calculated.

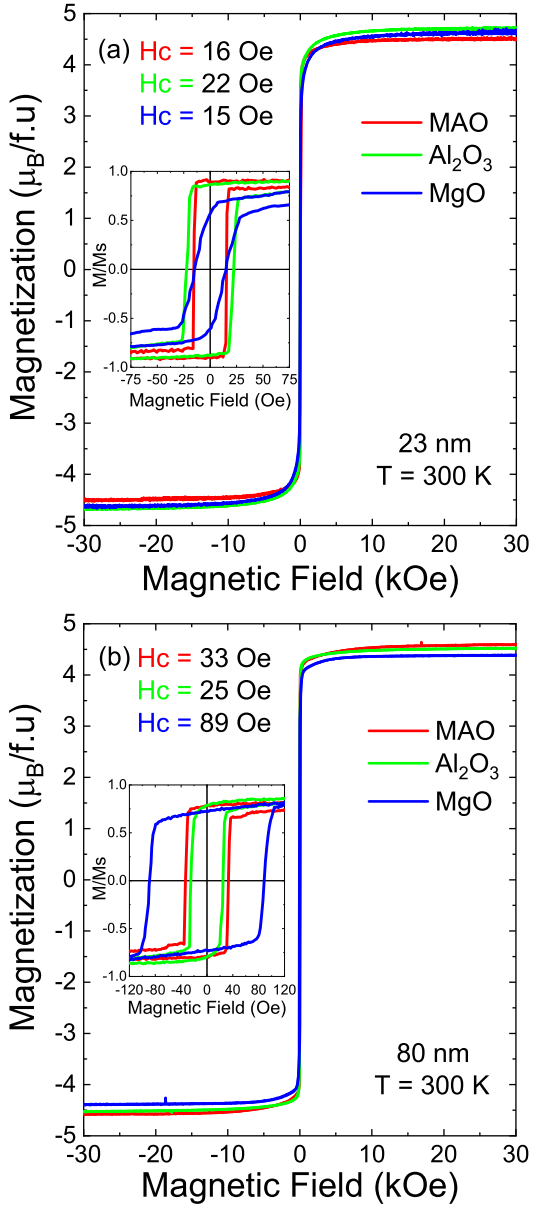

Fig. 10. Static magnetic hysteresis loops along $\Phi = 0°$ (i.e., along [100] substrate edge for MgO(001) and MAO(001) and along [0001] substrate edge for $Al_2O_3(11\bar{2}0)$) at 300 K for (a) 23 nm and (b) 80 nm thick CFTA thin films grown on MAO(001) (red), $Al_2O_3(11\bar{2}0)$ (green), and MgO(001) (blue) substrates.

From Fig. 7(a) and (b) we can see that CFTA films grown on MAO and MgO substrates seem to complete their transition from having equal IP and OP lattice parameters (6-–11 nm), to having a larger OP and smaller IP lattice parameter by 23 nm. At film thickness ≤ 11 nm, the CFTA films are tensile-strained with a relaxation shortly thereafter induced by some form of lattice distortion. The off-axis Φ scans as shown in Fig. 9(b) and (c) confirm the expected epitaxial orientation of CFTA thin films CFTA(001)[011]//MgO(001)[100] and CFTA(001)[011]//MAO(001)[100] by the four-fold crystallographic structural symmetry of CFTA(022) peaks with a 45° rotation to MgO(022) and MAO(044) peaks. We did not observe relevant XRD diffraction peaks for CFTA films grown on $Al_2O_3(11\bar{2}0)$ substrates in off-axis Φ scan measurement likely due to the columnar growth morphology as shown in Fig. 5(c)). Both IP and OP XRD measurements confirm phase pure, epitaxial films devoid of impurity peaks.

3.2. Magnetic properties

3.2.1. Static magnetic properties

The static magnetic properties for each CFTA thin film at room temperature were investigated using PPMS-VSM. The contribution from the substrate and the holder was removed by subtracting the high field linear background.

Fig. 10(a) and (b) show the IP (along the $\Phi = 0°$) static magnetic hysteresis loops for 23 nm and 80 nm thick CFTA film on MAO(001) (red), $Al_2O_3(11\bar{2}0)$ (green), and MgO(001) (blue) substrates. The magnetic saturation for 23 nm thick CFTA film is determined to be M_s = 865 ± 43 emu/cc (4.5 ±0.2μ_B/f.u. (where f.u. represents formula unit)), M_s = 889 ± 44 emu/cc (4.6 ±0.2μ_B/f.u.), and M_s = 895 ± 45 emu/cc (4.7 ±0.2μ_B/f.u.) respectively on MAO, MgO, and Al_2O_3 substrates. Similarly, for 80 nm thick film the magnetic saturation is determined to be M_s = 882 ± 44 emu/cc (4.6 ±0.2μ_B/f.u.), M_s = 840 ± 42 emu/cc (4.4 ±0.2μ_B/f.u.), and M_s = 860 ± 43 emu/cc (4.5 ±0.2μ_B/f.u.) respectively on MAO, MgO, and Al_2O_3 substrates. The observed saturation magnetic moment is smaller than 5.5 μ_B/f.u. predicted by the Slater-Pauling rule $M_t = Z_t$ - 24 [13], where Z_t is the number of valence electrons in the unit cell and much of the magnetic contribution in CFTA films should arise from the Fe and Co atoms. The reduction of magnetic moment in CFTA films could be due to defects or dislocations. We found a low coercivity (H_c) for our films except for the 80 nm thick film on the MgO substrate which could be due to the inhomogeneities acting as pinning centers. The observed coercivities are comparable to those observed by Gabor et al. [42] for MgO-buffered parent Co_2FeAl thin film. There have been no reports on CFTA thin films to our knowledge.

3.2.2. Dynamic magnetic properties

Broadband ferromagnetic resonance (FMR) spectroscopy at room temperature was used to investigate the dynamical magnetic properties of CFTA thin films. A custom-designed coplanar waveguide structure capable of operating up to 64 GHz [43] was employed for the measurements. A Schottky diode and lock-in detection [44] were used to measure the microwave power absorbed by the sample at a fixed frequency as a function of the applied field. An excellent signal-to-noise ratio can be obtained using this technique. The time evolution of the magnetization vector $\vec{M}$ in the presence of an effective field $\vec{H}_{eff}$ is described by the Landau–Lifshitz–Gilbert equation [45,46],

$$\frac{d\vec{M}}{dt} = -\gamma \vec{M} \times \vec{H}_{eff} + \frac{1}{M_s}\vec{M} \times \alpha_{eff}\frac{d\vec{M}}{dt} \quad (1)$$

where $\gamma = \frac{g\mu_B}{\hbar}$, M_s, and α_{eff} are the gyromagnetic ratio, saturation magnetization, and effective Gilbert damping parameter respectively. FMR measurements were carried out along $\Phi_H = 0°$ (applied field $\vec{H}$//[100] direction) and $\Phi_H = 45°$ (applied field $\vec{H}$//[011] for MgO and MAO substrates to determine IP easy and hard axes of the CFTA films with IP external magnetic and microwave field orthogonal to each other. Fig. 11(a) and (b) show exemplary FMR spectra - a first derivative of the absorption signal, for both IP and OP geometry for the 23 nm thick CFTA film on a MAO(001) substrate. The first derivative of the absorption signal is fitted using a Lorentzian lineshape [37] to extract the resonance field H_{res}, the center of the derivative curve, and peak-to-peak FMR linewidth ΔH_{pp}, the field width separation between the maximum and minimum of the derivative curve.

Both the IP ($\Phi_H = 0°$ and $\Phi_H = 45°$) and OP field dependencies of the resonant frequencies were considered to determine the gyromagnetic ratio and the effective magnetization. Fig. 12(a)–(c) show the Kittel plots for the 23 nm thick CFTA films on (a) MgO(001) (b) MAO(001), and (c) $Al_2O_3(11\bar{2}0)$ substrates. The experimental data were fitted using combined Kittel Eqs. (2) and (3) for IP easy and hard

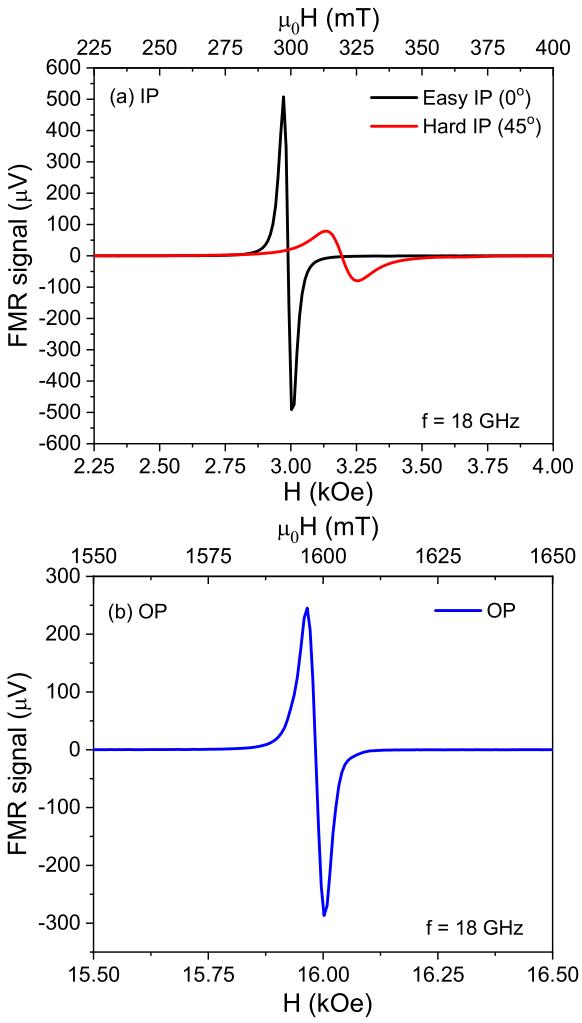

Fig. 11. FMR spectra at f = 18 GHz with the magnetic field H applied in both (a) in-plane (IP) and (b) out-of-plane (OP) direction to the film plane for the 23 nm thick CFTA film on MAO(001) substrate.

axes and OP assuming the magnetization vector aligns with the applied external field, i.e., $\Phi_H = \Phi_M$ for sufficiently large fields [47,48],

$$f_{IP} = \gamma' \left\{ [H_{res} + \frac{H_4}{2}cos(4(\Phi_H - \Phi_0^4)) + H_U cos(2(\Phi_H - \Phi_0^U))][H_{res} + \frac{H_4}{8}(3 + cos(4(\Phi_H - \Phi_0^4)) + \frac{H_U}{2}(1 + cos(2(\Phi_H - \Phi_0^U)) + 4\pi M_{eff}] \right\}^{1/2} \quad (2)$$

$$f_{OP} = \gamma' \left\{ H_{res} - 4\pi M_{eff} \right\} \quad (3)$$

where, H_4 describes an IP fourfold anisotropy, Φ_0^4 indicates the easy axis for $H_4 > 0$, H_U describes an IP uniaxial anisotropy, Φ_0^U indicates the easy axis for $H_U > 0$, and M_{eff} is the effective magnetization defined as $4\pi M_{eff} = 4\pi M_s + \frac{2K_\perp}{M_s}$, where $4\pi M_s$ is the demagnetization field and $K_\perp$ contains contributions from both a uniaxial perpendicular anisotropy and cubic anisotropy.

It should be noted that the reduced gyromagnetic ratio γ', M_{eff}, and H_4 are shared fit parameters. From the combined fit the reduced gyromagnetic ratio γ' was found to be 2.894 ± 0.002 GHz/kOe (2.895 ± 0.002 GHz/kOe) for the 23 nm thick CFTA film on MgO (MAO)(001) substrate. Similarly, it was found to be 2.914 ± 0.001 GHz/kOe for the 23 nm thick film on $Al_2O_3(11\bar{2}0)$ substrate. The

Table 1
Summary of reduced gyromagnetic ratio, damping parameter (extracted from out-of-plane (OP) data), inhomogeneous broadening (extracted from OP data), effective magnetization, and four fold anisotropy for 6 nm, 11 nm, 23 nm, and 40 nm thick CFTA films on MgO(001), MAO(001), and $Al_2O_3(11\bar{2}0)$ substrates.

Sample	Substrate	γ' (GHz/kOe)	α_{eff}	ΔH_0 (Oe)	M_{eff} (emu/cm^3)	H_4 (Oe)	H_u (Oe)
6 nm	MgO	2.894 ± 0.002	0.0032 ± 0.0002	35 ± 1	854 ± 1	346 ± 1	–
	MAO	2.886 ± 0.003	0.0029 ± 0.0001	37 ± 2	877 ± 2	348 ± 1	–
	Al_2O_3	2.8755 ± 0.0001	0.0040 ± 0.0003	25 ± 2	763 ± 2	–	80 ± 1
11 nm	MgO	2.885 ± 0.003	0.0018 ± 0.0002	45 ± 1	846 ± 2	335 ± 15	–
	MAO	2.885 ± 0.003	0.0020 ± 0.0001	24 ± 1	829 ± 2	348 ± 17	–
	Al_2O_3	2.892 ± 0.002	0.0020 ± 0.0001	11 ± 1	783 ± 1	-(19 ± 1)	126 ± 2
23 nm	MgO	2.894 ± 0.002	0.0024 ± 0.0001	22 ± 1	743 ± 1	253 ± 3	–
	MAO	2.895 ± 0.002	0.0025 ± 0.0001	11 ± 1	766 ± 1	256 ± 1	–
	Al_2O_3	2.914 ± 0.001	0.0019 ± 0.0002	15 ± 2	758 ± 1	−(24 ± 1)	164 ± 5
40 nm	MgO	2.93 ± 0.01	–	–	609 ± 1	221 ± 1	–
	MAO	2.922 ± 0.001	–	–	659 ± 1	198 ± 1	–
	Al_2O_3	2.8927 ± 0.0001	0.0039 ± 0.0002	0.25 ± 0.80	698 ± 1	19 ± 1	51 ± 1

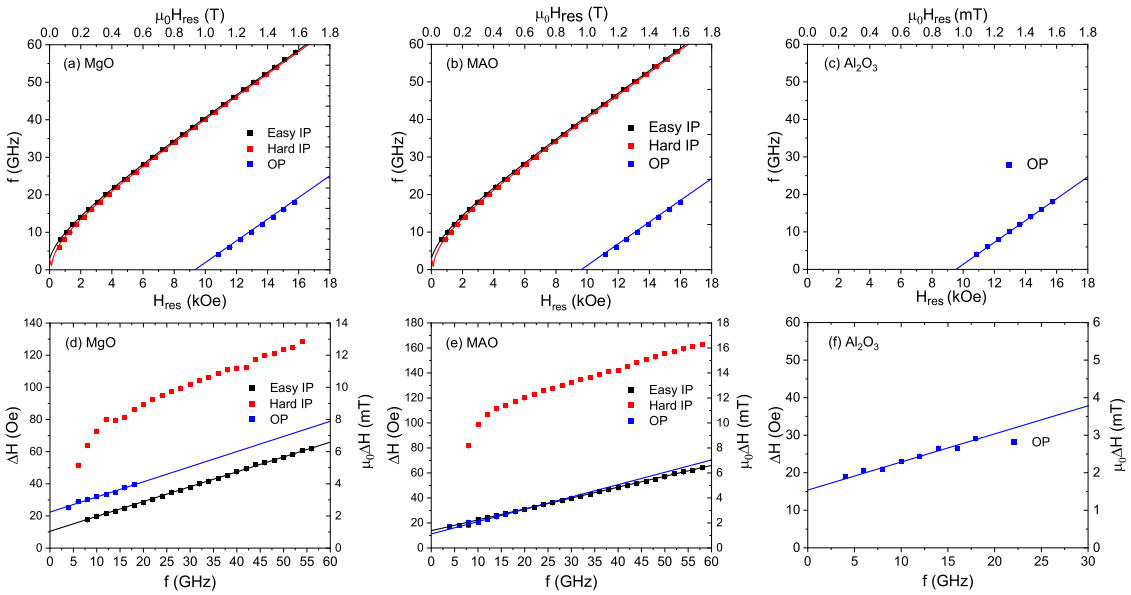

Fig. 12. Frequency versus resonance field (Kittel plot) along the in-plane (IP) easy (black), IP hard (red) magnetic axes, and out-of-plane (OP) (blue) direction for 23 nm thick CFTA film on (a) MgO(001) (b) MAO(001), and (c) $Al_2O_3(11\bar{2}0)$ substrate. The corresponding solid lines represent a combined Kittel fit Eq. (2) and Eq. (3) for IP and OP configuration to determine M_{eff} and γ'. Frequency dependent linewidth taken along the magnetic IP easy (black) and hard (red) axes and along OP direction (blue) for 23 nm thick CFTA on (d) MgO(001) (e) MAO(001), and (f) $Al_2O_3(11\bar{2}0)$ substrate. The corresponding solid lines represent the fit using Eq. (4) to extract the effective damping parameter. Kittel plot along IP directions is not shown for sample grown on $Al_2O_3(11\bar{2}0)$ substrate for the reason discussed in the text in context of Fig. 15.

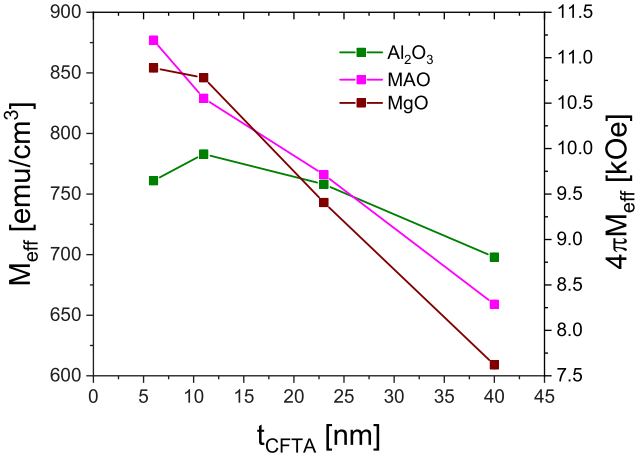

Fig. 13. Variation of effective magnetization (M_{eff}) with film thickness for CFTA films on different substrates.

corresponding effective magnetization M_{eff} was found to be 743 ± 1 emu/cc, 766 ± 1 emu/cc, and 758 ± 1 emu/cc for 23 nm thick CFTA film on MgO(001), MAO(001), and $Al_2O_3(11\bar{2}0)$ substrate. The observed effective magnetization is smaller than the saturation magnetization indicating the presence of perpendicular uniaxial anisotropy in the film. A four-fold anisotropy $H_4 = \frac{4K_4}{M_s}$ = 253 ± 3 Oe (256 ± 1 Oe) was observed for the 23 nm thick CFTA film on MgO (MAO)(001) substrate obtained from Kittel fits. The positive sign for H_4 indicates that $\Phi_H = 0°$ i.e., [100] direction (parallel to [011] direction of the film) is the easy axis of the film.

For CFTA films on $Al_2O_3(11\bar{2}0)$ substrates, the measurements were taken along $\Phi_H = 0°$ i.e., $\overrightarrow{H}$//[0001] direction. To determine the effective Gilbert parameter α_{eff}, the extracted linewidth ΔH_{pp} is plotted as a function of microwave frequency, f, [49–51]. Fig. 12(d)–(e) show the frequency dependency of the linewidth for fields applied in both IP (easy and hard axes) and OP configurations for 23 nm thick CFTA film grown on (a) MgO(001) (b) MAO(001) substrates, and Fig. 12(f) shows the frequency dependency for OP configuration for 20 nm thick CFTA film grown on $Al_2O_3(11\bar{2}0)$ substrate. We observe an increase in linewidth with frequency. For films on the substrates with four-fold symmetry, a linear dependence of linewidth is seen for OP geometry

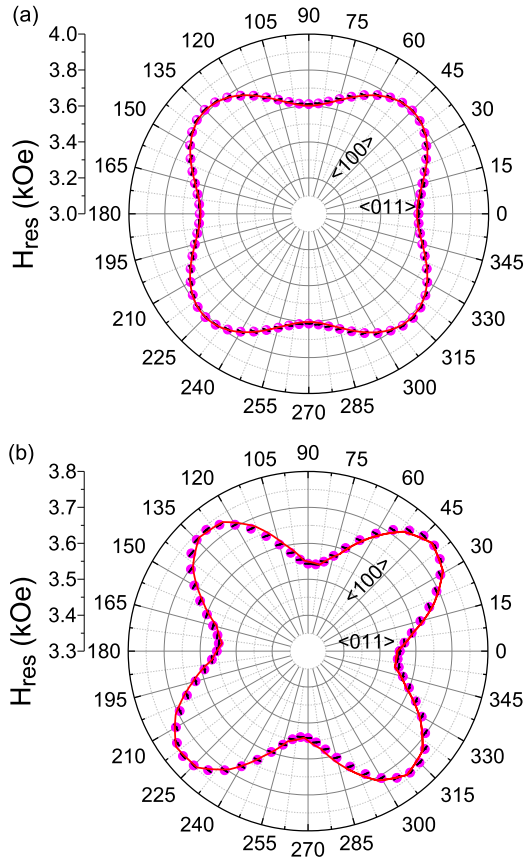

Fig. 14. In-plane angular dependence of resonance fields (magenta) H_{res} demonstrating four-fold anisotropy with <110> being the easy axis of the 23 nm thick CFTA film on (a) MgO(001) and (b) MAO(001) substrates measured at a microwave frequency of 20 GHz. The resonant fields are fitted (red solid line) to extract the four-fold anisotropy term H_4. (*Given crystallographic directions correspond to the film.)*.

and along the easy IP axes. The non-linearity observed along the hard IP axes could be due to a significant contribution from two-magnon scattering. As can be seen, Fig. 12(d)–(f) the frequency dependence of the linewidth for all samples for the OP configuration is well described by a linear relationship,

$$\Delta H(f) = \Delta H_0 + \frac{2}{\sqrt{3}}\frac{\alpha_{eff}}{\gamma'} f \quad (4)$$

where ΔH_0 is the inhomogeneous broadening. If the magnetization aligns with the applied external field, then there is no contribution to the linewidth from field dragging. However, one cannot rule out the possible contribution originating from spin pumping [52,53], eddy currents [54], and for the IP measurements, two-magnon scattering which can scale approximately linearly with frequency [49,55–57]. To sum up these contributions we use the term "effective Gilbert damping parameter", α_{eff}. The inhomogeneous linewidth broadening was found to be ΔH_0 = 11 ± 1 Oe and 15.4 ± 1.5 Oe for 11 nm and 23 nm film on $Al_2O_3(11\bar{2}0)$ substrate. Whereas, on MgO (MAO)(001) substrate ΔH_0 = 45 ± 1 Oe (24 ± 1 Oe) and 22.3 ± 1.0 Oe (11 ± 1 Oe) were obtained for 11 nm and 23 nm thick CFTA films respectively. These observed values of ΔH_0 are comparable to those obtained by Belmeguenai et al. for Co_2FeAl thin films [58]. A low effective Gilbert damping parameter, α_{eff} ~0.0020 was found for 11 nm and 23 nm thick CFTA films across all substrates. The values for the reduced gyromagnetic ratio, damping parameter, linewidth, effective magnetization, four-fold anisotropy, and the uniaxial anisotropy terms are summarized in Table 1. We observe that M_{eff} decreases gradually with increasing film thickness as shown in Table 1 and in Fig. 13. This can likely be attributed to strain relaxation in thicker films in accordance with lattice parameter evolution as shown in Fig. 7. Further, there could be Co/Fe rich interfacial region as well as oxidation of Al in the thinner films that would likely explain the higher value of magnetization in thinner films as shown in Fig. 13.

Fig. 14(a) and (b) show the IP angular dependence of the resonant field H_{res} for the 23 nm thick CFTA films on MgO(001) and MAO(001) substrates, respectively. The FMR IP rotational measurements were carried out at a fixed frequency of 20 GHz at room temperature. A clear four-fold magnetic anisotropy is visible in Fig. 14 and is consistent with the crystallographic four-fold symmetry. The four-fold anisotropy H_4 was determined by fitting the experimental data using Eq. (2). Fig. 15 shows the IP angular dependence of the resonant field H_{res} for 23 nm thick CFTA film on $Al_2O_3(11\bar{2}0)$ substrate suggesting a strong uniaxial anisotropy (two-fold symmetry). This uniaxial anisotropy observed is consistent with two-fold symmetry of the $(11\bar{2}0)$ plane of the $Al_2O_3(11\bar{2}0)$ substrate. For the 6 nm thick film, the easy axis of the uniaxial anisotropy aligns with Φ_H = 0°, but as shown in Fig. 15 we observe a gradual change in the IP alignment of ~ 15° with an increase in thickness. This rotation could possibly be due to the competition between an anisotropic growth morphology induced uniaxial anisotropy and uniaxial anisotropy due to two-fold crystal symmetry. The increasing misalignment of the easy axis with respect to the [001] axis of $Al_2O_3(11\bar{2}0)$ substrate in this scenario would indicate a change of the growth morphology induced uniaxial anisotropy with increasing film thickness. Additionally, the relaxation of the CFTA films by ~40 nm thickness, as observed by XRD, may potentially indicate a relaxation-induced lattice distortion pointing in the same in-plane direction. In such a picture, relaxation of the dense, compressively strained film would require a uniaxial distortion and that would realign the easy axis as we observe in Fig. 15.

4. Conclusion

We investigated the structural and dynamic magnetic properties of phase pure, epitaxial CFTA thin films of various thicknesses (t = 6 nm, 11 nm, 23 nm, 40 nm, 57 nm, and 80 nm) grown on cubic MgO(001), MAO(001), and $Al_2O_3(11\bar{2}0)$ substrates by combinatorial sputter beam epitaxy. From the microstructure analysis, a uniformly oriented epitaxial crystal was observed on films grown on MgO substrate whereas a columnar growth mode with distinct high-angle grain boundaries was observed for films grown on $Al_2O_3(11\bar{2}0)$ substrate. A four-fold crystallographic anisotropy was observed for films grown on cubic substrates. A low coercivity was observed across all films on all substrates and a saturation magnetic moment of ~5 μ_B/formula unit was observed for our films. The IP polar plot for the film on $Al_2O_3(11\bar{2}0)$ substrates showed a very strong uniaxial anisotropy, whereas FMR verified a four-fold magnetic anisotropy for films grown on the cubic substrates. Additionally, low inhomogeneous linewidth contribution and effective damping parameters were obtained for CFTA films on MgO(001), MAO(001), and $Al_2O_3(11\bar{2}0)$ substrates. These results may indicate potential compatibility with high-frequency device applications.

CRediT authorship contribution statement

Sujan Budhathoki: Conceptualization, Methodology, Writing – original draft, Investigation. **Anish Rai:** Data curation, Investigation. **Ka Ming Law:** Visualization, Investigation. **Ridwan Nahar:** Data curation, Investigation. **Andrew Stewart:** Data curation, Investigation. **Smriti Ranjit:** Investigation, Writing – reviewing & editing. **Shambhu K.C.:** Conceptualization, Methodology, Software. **Tamara Isaacs-Smith:** Data curation, Writing – original draft. **Ilias Bikmukhametov:** Data curation, Visualization, Investigation. **Ryan B. Comes:** Supervision, Writing – reviewing & editing. **Gregory B. Thompson:** Supervision. **Patrick R. LeClair:** Writing – reviewing & editing. **Tim Mewes:** Supervision, Writing – reviewing & editing. **Adam J. Hauser:** Data curation, Writing – reviewing & editing, Methodology, Conceptualization, Project administration, Funding acquisition.

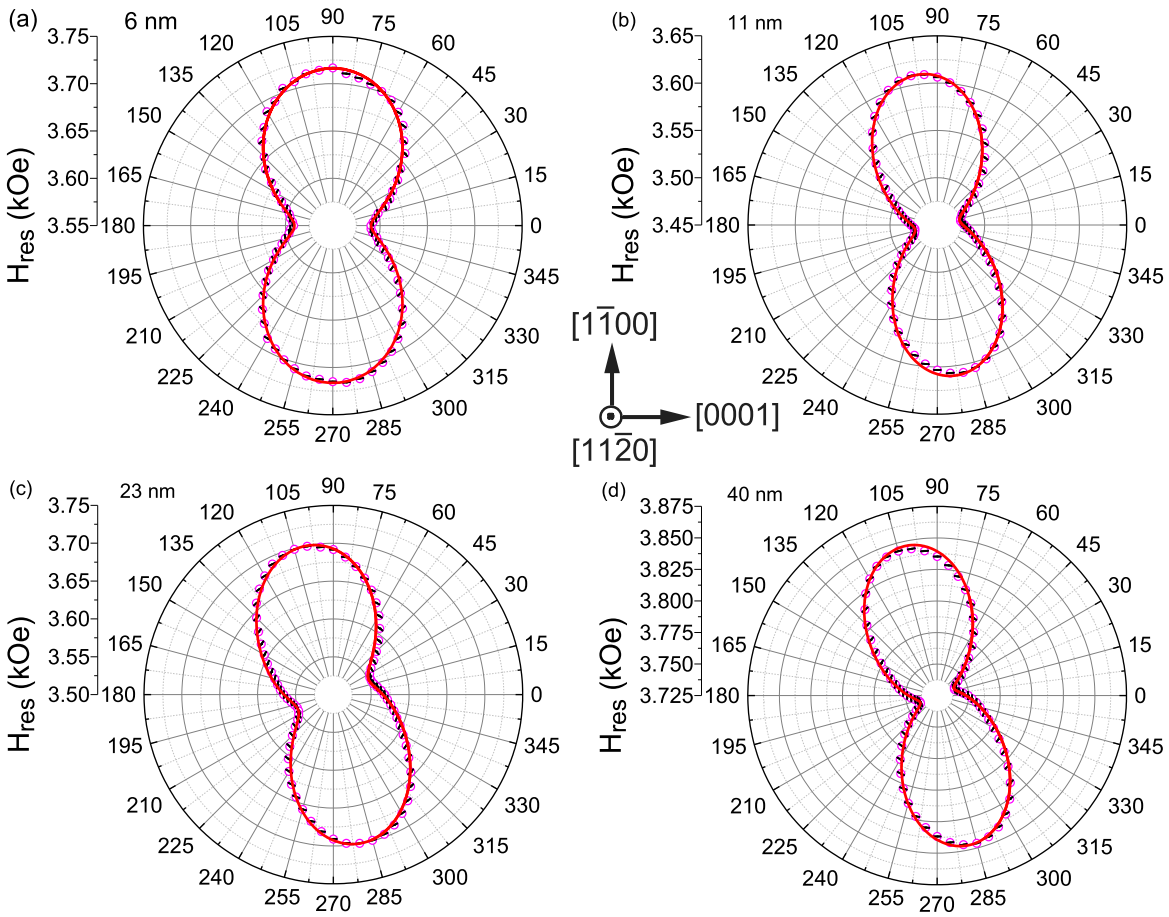

Fig. 15. In-plane angular dependence of resonance fields (magenta) H_{res} demonstrating a strong uniaxial anisotropy across (a) 6 nm, (b) 11 nm, (c) 23 nm, and (d) 40 nm thick CFTA films on $Al_2O_3(11\bar{2}0)$ substrate measured at a microwave frequency of 20 GHz. The red solid curve represents the fit curve to extract uniaxial anisotropy term H_U. The data were fitted using the implicit formula of Eq. (2), where Φ_0^U was taken as a free parameter. The easy axis [001] shifts by ~ 15° at most taking into account the uniaxial anisotropy H_U.

Declaration of competing interest

The authors declare that they have no known competing financial interests or personal relationships that could have appeared to influence the work reported in this paper.

Data availability

Data will be made available on request.

Acknowledgments

S.B, R.N, and A.J.H acknowledge support from the National Science Foundation (NSF), USA through NSF-CAREER Award No. DMR-2047251. R.B.C acknowledges support from the National Science Foundation (NSF), USA through NSF-DMR-1809847. Alabama Analytical Research Center (AARC) at the University of Alabama is acknowledged for the use of the SEM/FIB and TEM instruments.

References

[1] E. Myers, D. Ralph, J. Katine, R. Louie, R. Buhrman, Science 285 (5429) (1999) 867–870.
[2] L. Liu, C.-F. Pai, Y. Li, H. Tseng, D. Ralph, R. Buhrman, Science 336 (6081) (2012) 555–558.
[3] A.J. Lee, J.T. Brangham, Y. Cheng, S.P. White, W.T. Ruane, B.D. Esser, D.W. McComb, P.C. Hammel, F. Yang, Nature Commun. 8 (1) (2017) 1–6.
[4] J.C. Slonczewski, et al., J. Magn. Magn. Mater. 159 (1) (1996) L1.
[5] T. Graf, C. Felser, S.S. Parkin, Prog. Solid State Chem. 39 (1) (2011) 1–50.
[6] C. Felser, A. Hirohata, Heusler Alloys, Springer, 2015.
[7] R. De Groot, F. Mueller, P. Van Engen, K. Buschow, Phys. Rev. Lett. 50 (25) (1983) 2024.
[8] J. Wernick, G. Hull, T. Geballe, J. Bernardini, J. Waszczak, Mater. Lett. 2 (2) (1983) 90–92.
[9] S. Chadov, X. Qi, J. Kübler, G.H. Fecher, C. Felser, S.C. Zhang, Nature Mater. 9 (7) (2010) 541–545.
[10] S. Trudel, O. Gaier, J. Hamrle, B. Hillebrands, J. Phys. D: Appl. Phys. 43 (19) (2010) 193001.
[11] S. Wurmehl, G.H. Fecher, H.C. Kandpal, V. Ksenofontov, C. Felser, H.-J. Lin, J. Morais, Phys. Rev. B 72 (18) (2005) 184434.
[12] P. Brown, K.-U. Neumann, P. Webster, K. Ziebeck, J. Phys.: Condens. Matter 12 (8) (2000) 1827.
[13] I. Galanakis, P.H. Dederichs, N. Papanikolaou, Phys. Rev. B 66 (2002) 174429.
[14] G.H. Fecher, H.C. Kandpal, S. Wurmehl, C. Felser, G. Schönhense, J. Appl. Phys. 99 (8) (2006) 08J106.
[15] S. Wurmehl, G.H. Fecher, H.C. Kandpal, V. Ksenofontov, C. Felser, H.-J. Lin, Appl. Phys. Lett. 88 (3) (2006) 032503.
[16] W. Wang, H. Sukegawa, R. Shan, S. Mitani, K. Inomata, Appl. Phys. Lett. 95 (18) (2009) 182502.
[17] W. Wang, E. Liu, M. Kodzuka, H. Sukegawa, M. Wojcik, E. Jedryka, G. Wu, K. Inomata, S. Mitani, K. Hono, Phys. Rev. B 81 (14) (2010) 140402.
[18] S. Mizukami, D. Watanabe, M. Oogane, Y. Ando, Y. Miura, M. Shirai, T. Miyazaki, J. Appl. Phys. 105 (7) (2009) 07D306.
[19] C. Liu, C.K. Mewes, M. Chshiev, T. Mewes, W.H. Butler, Appl. Phys. Lett. 95 (2) (2009) 022509.
[20] R. Yilgin, Y. Sakuraba, M. Oogane, S. Mizukami, Y. Ando, T. Miyazaki, Japan. J. Appl. Phys. 46 (3L) (2007) L205.
[21] M. Oogane, T. Wakitani, S. Yakata, R. Yilgin, Y. Ando, A. Sakuma, T. Miyazaki, Japan. J. Appl. Phys. 45 (5R) (2006) 3889.
[22] C. Cheng, K. Meng, S. Li, J. Zhao, T. Lai, Appl. Phys. Lett. 103 (23) (2013) 232406.
[23] K. Meng, S. Wang, P. Xu, L. Chen, W. Yan, J. Zhao, Appl. Phys. Lett. 97 (23) (2010) 232506.

[24] S. Wurmehl, M.C.M. Alves, J. Morais, V. Ksenofontov, S.R. Teixeira, G. Machado, G.H. Fecher, C. Felser, J. Phys. D: Appl. Phys. 40 (6) (2007) 1524.
[25] L. Basit, G.H. Fecher, S. Chadov, B. Balke, C. Felser, Eur. J. Inorg. Chem. 2011 (26) (2011) 3950.
[26] N. Tezuka, N. Ikeda, S. Sugimoto, K. Inomata, Japanese J. Appl. Phys. 46 (5L) (2007) L454.
[27] B. Peters, A. Alfonsov, C. Blum, S.J. Hageman, P. Woodward, S. Wurmehl, B. Büchner, F. Yang, Appl. Phys. Lett. 103 (16) (2013) 162404.
[28] L.M. Loong, J.H. Kwon, P. Deorani, C.N. Tung Yu, A. Hirohata, H. Yang, Appl. Phys. Lett. 104 (23) (2014) 232409.
[29] S. Budhathoki, A. Sapkota, K.M. Law, S. Ranjit, B. Nepal, B.D. Hoskins, A.S. Thind, A.Y. Borisevich, M.E. Jamer, T.J. Anderson, et al., Phys. Rev. B 101 (22) (2020) 220405(R).
[30] S. Budhathoki, A. Sapkota, K.M. Law, B. Nepal, S. Ranjit, K. Shambhu, T. Mewes, A.J. Hauser, J. Magn. Magn. Mater. 496 (2020) 165906.
[31] K.M. Law, S. Budhathoki, S. Ranjit, F. Martin, A.S. Thind, R. Mishra, A.J. Hauser, Sci. Rep. 10 (1) (2020) 1–10.
[32] S. Budhathoki, A. Sapkota, K.M. Law, S. Ranjit, G.M. Stephen, D. Heiman, M.E. Jamer, T. Mewes, A.J. Hauser, J. Magn. Magn. Mater. 564 (2022) 170053.
[33] J.M. Shaw, H.T. Nembach, T.J. Silva, J. Appl. Phys. 108 (9) (2010) 093922.
[34] L.A. Giannuzzi, F.A. Stevie, Micron 30 (3) (1999) 197–204.
[35] J. Brons, G. Thompson, JOM 66 (1) (2014) 165–170.
[36] G. Bergerhoff, I. Brown, F. Allen, et al., Int. Union Crystallogr., Chester 360 (1987) 77–95.
[37] C. Oates, F. Ogrin, S. Lee, P. Riedi, G. Smith, T. Thomson, J. Appl. Phys. 91 (3) (2002) 1417–1422.
[38] J. Ayers, J. Cryst. Growth 135 (1–2) (1994) 71–77.
[39] P.F. Miceli, C. Palmstro, et al., Phys. Rev. B 51 (8) (1995) 5506.
[40] A. Kortan, M. Hong, J. Kwo, J. Mannaerts, N. Kopylov, Phys. Rev. B 60 (15) (1999) 10913.
[41] P. Webster, J. Phys. Chem. Solids 32 (6) (1971) 1221–1231.
[42] M. Gabor, T. Petrisor Jr., C. Tiusan, M. Hehn, T. Petrisor, Phys. Rev. B 84 (13) (2011) 134413.
[43] S. Keshavarz, Y. Xu, S. Hrdy, C. Lemley, T. Mewes, Y. Bao, IEEE Trans. Magn. 46 (6) (2010) 1541–1543.
[44] C. Pang, A. Srivastava, M.M. Lockart, T. Mewes, M.K. Bowman, N. Bao, L. Shen, A. Gupta, ACS Appl. Electron. Mater. (2019).
[45] T.L. Gilbert, IEEE Trans. Magn. 40 (6) (2004) 3443–3449.
[46] A. Aharoni, et al., Introduction to the Theory of Ferromagnetism, Vol. 109, Clarendon Press, 2000.
[47] Y.V. Goryunov, N. Garif'yanov, G. Khaliullin, I. Garifullin, L. Tagirov, F. Schreiber, T. Mühge, H. Zabel, Phys. Rev. B 52 (18) (1995) 13450.
[48] M. Belmeguenai, F. Zighem, Y. Roussigné, S. Chérif, P. Moch, K. Westerholt, G. Woltersdorf, G. Bayreuther, Phys. Rev. B 79 (2) (2009) 024419.
[49] C.K. Mewes, T. Mewes, Handb. Nanomagnetism: Appl. Tools (2015) 71–96.
[50] B. Heinrich, J. Cochran, R. Hasegawa, J. Appl. Phys. 57 (8) (1985) 3690–3692.
[51] R.D. McMichael, D. Twisselmann, A. Kunz, Phys. Rev. Lett. 90 (22) (2003) 227601.
[52] Y. Tserkovnyak, A. Brataas, G.E. Bauer, Phys. Rev. Lett. 88 (11) (2002) 117601.
[53] A. Rai, A. Sapkota, A. Pokhrel, M. Li, M. De Graef, C. Mewes, V. Sokalski, T. Mewes, Phys. Rev. B 102 (2020) 174421.
[54] N.S. Almeida, D.L. Mills, Phys. Rev. B 53 (18) (1996) 12232.
[55] G. Woltersdorf, B. Heinrich, Phys. Rev. B 69 (18) (2004) 184417.
[56] S. Wu, K. Abe, T. Nakano, T. Mewes, C. Mewes, G. Mankey, T. Suzuki, Phys. Rev. B 99 (14) (2019) 144416.
[57] A. Rai, M. Dunz, A. Sapkota, P. Zilske, J.B. Mohammadi, M. Meinert, C. Mewes, T. Mewes, J. Magn. Magn. Mater. 485 (2019) 374–380.
[58] M. Belmeguenai, H. Tuzcuoglu, M. Gabor, T. Petrisor Jr., C. Tiusan, D. Berling, F. Zighem, T. Chauveau, S. Chérif, P. Moch, Phys. Rev. B 87 (18) (2013) 184431.